Controlled skyrmion ratchet in linear protrusion defects

J. C. Bellizotti Souza [1] N. P. Vizarim [2] C. J. O. Reichhardt [3] C. Reichhardt [3] and P. A. Venegas [2]

[1]*POSMAT - Programa de Pós-Graduação em Ciência e Tecnologia de Materiais, Faculdade de Ciências,*
Universidade Estadual Paulista - UNESP, Bauru, SP, CP 473, 17033-360, Brazil
[2]*Departamento de Física, Faculdade de Ciências, Unesp-Universidade Estadual Paulista, CP 473, 17033-360 Bauru, SP, Brazil*
[3]*Theoretical Division and Center for Nonlinear Studies, Los Alamos National Laboratory, Los Alamos, New Mexico 87545, USA*

Using atomistic simulations, we investigate the dynamical behavior of a single skyrmion interacting with an asymmetric linear protrusion array under external ac driving. The linear protrusion array is placed in the xy plane and is composed of magnetic walls near the edge of the nanotrack that have angled linear protrusions into the nanotrack. The structure forms a hard axis for $-x$ direction motion and an easy axis for $+x$ direction motion. When the ac drive is applied along the x direction, the skyrmion moves along the hard direction of the substrate asymmetry in three phases: a pinned phase with localized skyrmion orbits, a constant velocity phase where the orbits become delocalized, and a reentrant pinned phase with larger localized orbits. We measure the dependence of the skyrmion velocity on the frequency and amplitude of the ac drive. All three phases appear for all frequency values simulated here, and in the constant velocity phase the skyrmion velocity depends only on the frequency and not on the amplitude of the ac drive. When ac driving is applied in the y direction, the skyrmion moves along the easy direction of the substrate asymmetry and exhibits the same three phases as for x-direction driving along with a fourth phase which, at high driving frequencies, consists of a series of constant velocity phases, each with different average skyrmion velocities. For low frequencies, the constant velocity phase is lost and the skyrmion speed increases linearly with increasing ac drive amplitude due to a Magnus boost effect. Our findings suggest new ways to create reliable data transport for spintronic devices using skyrmions as information carriers, where the skyrmion direction and speed can be controlled by varying only the ac drive amplitude and frequency.

I. INTRODUCTION

In the field of data storage, there is great interest in discovering novel approaches that demand lower energy consumption and offer increased data density. The rapid increase in cloud-based storage has resulted in substantial energy consumption [1], a concern that can be mitigated through new data storage techniques capable of enhancing data density and data transfer efficiency. One promising direction is to employ topological stable objects with reduced dimensions whose transport can be controlled precisely. Recently magnetic skyrmions, which are topologically stable spin textures [2,3] of size ranging from a few nanometers up to a micrometer [4], have been observed experimentally in chiral ferromagnetic thin films and bulk crystals [5–8]. Skyrmions are considered one of the most promising candidates for future spintronic devices [2,9,10] due to their reduced size and stability even at room temperatures [10,11], as well as their ability to be transported via the application of a spin-polarized current. The current density necessary to drive a skyrmion is over five orders of magnitude smaller than that required to move magnetic domain walls [12,13], and as a result, skyrmion-based devices could provide more reliable and energy-efficient high-density data storage. Some of the proposed skyrmion-based devices include magnetic logic gates [14–16], diodes [15,17–22], and transistors [23]. Magnetic skyrmions could also be used in nonconventional computing, such as audio classification artificial intelligence [24] and neuromorphic computing [20,25,26]. In order

to harness magnetic skyrmions effectively for spintronics devices and unconventional computing, precise control over their motion is crucial, and significant efforts have been devoted to achieve this goal [10,27–32].

Skyrmions exhibit many similarities to other overdamped particles. Both minimize their repulsive interactions by forming a triangular lattice, can be set into motion by external drives, and interact with defects in the material [33,34]. A distinguishing property of skyrmions is the presence of a strong nondissipative Magnus force, which results in a very distinct dynamical behavior since the Magnus force creates a velocity component perpendicular to the net force acting on the skyrmion. The sign of this perpendicular component depends on the skyrmion winding number or topological charge [2,35–40]. Due to the presence of the Magnus term, the skyrmion moves at what is known as the intrinsic skyrmion Hall angle θ_{sk}^{int} [2,35–39] with respect to an applied external drive. The intrinsic skyrmion Hall angle is an important problem for technological applications, since it can cause skyrmions to move towards the edge of the sample, leading to annihilation events that limit how far the skyrmion can travel. In order to prevent this annihilation process, a precise control of the skyrmion motion is required. There is an increased effort to find new ways to control the skyrmion motion and avoid the intrinsic skyrmion Hall angle problem. Some of the proposed methods include the use of periodic pinning [41–46], sample curvature [47–49], interface guided motion [50,51], ratchet effects [52–55], temperature and magnetic gradients [56–59],
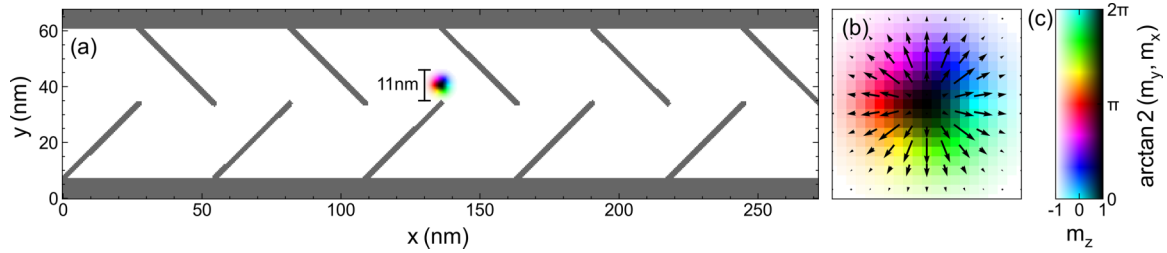
FIG. 1. (a) Illustration of the sample considered in this work with walls and linear protrusions (gray) that are generated using very strong perpendicular magnetic anisotropy (PMA). The colored disk represents the skyrmion. (b) A blowup of the Néel skyrmion spin texture in the x-y plane from (a), highlighting the magnetic moment components m_x and m_y. (c) The color map used is based on the relative angle of m_x and m_y, while the brightness level is determined by the value of m_z.

granular films [60], parametric pumping [61], skyrmion-vortex coupling using heterostructures [62,63], skyrmion lattice compression [64,65], laminar flow of skyrmions [28], soliton motion along skyrmion chains [66,67], and skyrmions interacting with chiral flowers [68].

The interaction of overdamped particles with asymmetric potentials under dc or ac driving has been explored widely [52,69–77]. For ac driving, the system may exhibit a ratchet effect in which there is a net dc transport of the particle that is generally along the easy flow direction of the potential. One of the earliest skyrmion ratchet studies involved a quasi-one-dimensional (quasi-1D) asymmetric substrate [52]. For ac drives applied parallel to the substrate asymmetry direction, quantized net dc displacements of the skyrmion occurred, while a Magnus-induced transverse ratchet appeared when the ac driving was perpendicular to the substrate asymmetry direction. In recent work, Souza *et al.* [53] proposed a device where the motion of a single magnetic skyrmion interacting with an asymmetric funnel array could be precisely controlled, providing an information carrier. With this geometry, it was possible to produce ratcheting motion of the skyrmion along both the easy and hard substrate asymmetry directions; however, the motion in the hard direction had low efficiency.

Another example of asymmetric arrays is the linear protrusion array, shown in Fig. 1, which was previously used for type II superconducting vortices by Wells [78]. In that work, an external dc driving force was employed to induce a vortex diode effect. The depinning threshold was low for driving currents applied along the easy flow direction and high for driving along the hard flow direction. Wells argued that ac driving would induce a vortex ratchet effect. Here, we perform a detailed analysis of the behavior of magnetic skyrmions in a linear protrusion array, focusing on the ratchet effects that arise under ac driving with varied amplitude and frequency.

In this work we show that when the ac drive is applied along the x direction, the skyrmion exhibits three dynamical phases: (i) a pinned phase (PP), (ii) a constant velocity phase (CVP) with motion along the hard substrate asymmetry direction, and (iii) a reentrant pinned phase (RPP). Within the CVP, we find that the skyrmion velocity depends exclusively on the ac driving frequency. In addition, the interval of ac drive amplitudes for which the CVP appears varies with the driving frequency. When we apply the ac drive along the y direction, we uncover a more complex behavior featuring four phases: (i) PP, (ii) CVP with motion along the easy substrate asymmetry direction, (iii) RPP, and (iv) a mixture of CVP and

a linear increase of the skyrmion velocity with increasing ac amplitude. Each phase appears within a well-defined range of ac amplitude and frequency. The velocity characteristics in the CVP state mirror those observed for ac driving along the x direction, with the velocity being determined exclusively by the ac frequency. In the fourth phase, a succession of CVPs with distinct average skyrmion velocities emerges at higher ac drive frequencies, while for lower frequencies, the CVP dissipates and the skyrmion velocity increases linearly with the ac drive amplitude. A precise control of the skyrmion motion can be achieved by tailoring the ranges of ac amplitude and frequency in order to guide the skyrmion in a desired fashion.

II. SIMULATION

The sample considered here is an ultrathin nanotrack of ferromagnetic material that can host Néel skyrmions. The nanotrack has dimensions of 272 nm × 64 nm and a magnetic field is applied perpendicular to the film surface at $T = 0$ K. Periodic boundary conditions are applied only along the x direction. The sample contains magnetic walls close to the sample edge and a linear protrusion array of defects, where the magnetic moments that compose the walls and the linear protrusion array have very strong perpendicular magnetic anisotropy (PMA). We introduce the walls in order to confine the skyrmions along the nanotrack. Throughout this work we always consider the dynamics of a single skyrmion, and the initial skyrmion configuration is illustrated in Fig. 1.

We use an atomistic model [79] for the simulations to investigate the skyrmion spin textures in detail. The Hamiltonian governing the spin dynamics is given by [36,80,81]:

$$\mathscr{H} = -\sum_{i,j\in N} J_{i,j}\mathbf{m}_i \cdot \mathbf{m}_j - \sum_{i,j\in N} \mathbf{D}_{i,j} \cdot (\mathbf{m}_i \times \mathbf{m}_j) - \sum_i \mu \mathbf{H} \cdot \mathbf{m}_i - \sum_i K_1(\mathbf{m}_i \cdot \hat{\mathbf{z}})^2. \quad (1)$$

The first term on the right side is the exchange interaction between the nearest neighbors that compose the set N. The underlying lattice is a square spin lattice with lattice constant a and exchange constant $J_{i,j}$ between spins i and j. The second term is the interfacial Dzyaloshinskii-Moriya interaction, where $\mathbf{D}_{i,j}$ is the Dzyaloshinskii-Moriya vector between spins i and j. The third term is the spin interaction with an external

applied magnetic field $\mathbf{H}$ known as the Zeeman interaction, where $\mu = \hbar\gamma$ is the magnetic moment magnitude and $\gamma = 1.76 \times 10^{11}$ T^{-1}s^{-1} is the electron gyromagnetic ratio. The last term is the sample easy-axis anisotropy, where K_1 is the anisotropy strength. We model the set of spins L that compose the linear protrusion array of defects as fixed magnetic moments, $\mathbf{m}_{\in L} = -\hat{\mathbf{z}}$, and we note that if we replace these fixed moments by defects with very strong PMA values K_L, such as $K_L = 5J$, we obtain the same result that the motion of skyrmions through the defects is prevented [82]. Long-range dipolar interactions are neglected in our simulations since they are expected to be very small for ultrathin films [83].

The time evolution for the magnetic moments follows the LLG equation augmented with the adiabatic spin transfer torque [81,84,85]:

$$\frac{\partial \mathbf{m}_i}{\partial t} = -\gamma \mathbf{m}_i \times \mathbf{H}_i^{\text{eff}} + \alpha \mathbf{m}_i \times \frac{\partial \mathbf{m}_i}{\partial t} + \frac{pa^3}{2e}(\mathbf{j} \cdot \nabla)\mathbf{m}_i. \quad (2)$$

Here, γ is the gyromagnetic ratio, $\mathbf{H}_i^{\text{eff}} = -\frac{1}{\hbar\gamma}\frac{\partial \mathcal{H}}{\partial \mathbf{m}_i}$ is the effective field including all interactions in the Hamiltonian, α is the phenomenological damping term introduced by Gilbert, and the last term is the spin-transfer torque (STT), where p is the spin polarization, e the electron charge, and $\mathbf{j}$ the applied current density. The STT current includes the assumption that conduction electron spins are always parallel to the magnetic moments $\mathbf{m}$ [36,86]. We only consider the adiabatic contribution from the current interaction. Nonadiabatic contributions are usually weak in ferromagnets; however, in special cases, such as Weyl ferromagnets [87,88], the nonadiabatic terms can be strong and affect the skyrmion dynamics. Here, nonadiabatic contributions can be neglected since they do not affect the skyrmion dynamics significantly under small driving forces [35]. We use an alternating STT current given by

$$\mathbf{j} = j_x \cos(2\pi\omega t)\hat{\mathbf{x}} + j_y \sin(2\pi\omega t)\hat{\mathbf{y}}, \quad (3)$$

where ω is the oscillating frequency, t is the time, and j_x and j_y are the current amplitudes in the x and y directions, respectively.

The skyrmion velocity is calculated using the emergent electromagnetic fields [12,81]:

$$E_i^{\text{em}} = \frac{\hbar}{e}\mathbf{m} \cdot \left(\frac{\partial \mathbf{m}}{\partial i} \times \frac{\partial \mathbf{m}}{\partial t}\right)$$

$$B_i^{\text{em}} = \frac{\hbar}{2e}\varepsilon_{ijk}\mathbf{m} \cdot \left(\frac{\partial \mathbf{m}}{\partial j} \times \frac{\partial \mathbf{m}}{\partial k}\right), \quad (4)$$

where ε_{ijk} is the totally antisymmetric tensor. The skyrmion drift velocity is then computed using $\mathbf{E}^{\text{em}} = -\mathbf{v}_d \times \mathbf{B}^{\text{em}}$ [12,81].

In our simulations we fix $\mu\mathbf{H} = 0.5(D^2/J)(-\hat{\mathbf{z}})$, $\alpha = 0.3$, $p = -1.0$, and $a = 0.5$ nm, and we consider $J = 1$ meV, $D = 0.18J$, and $K = 0.02J$, which are magnetic parameters that stabilize Néel skyrmions similar to those found for Pt/Co/MgO ultrathin films [90]. All our simulations start from the spin configuration shown in Fig. 1. The numerical integration of Eq. (2) is performed using a fourth-order Runge-Kutta method. For each value of the ac drive amplitude, we calculate the time-averaged skyrmion velocities along the x direction, $\langle v_x \rangle$, over 3×10^7 time steps to ensure
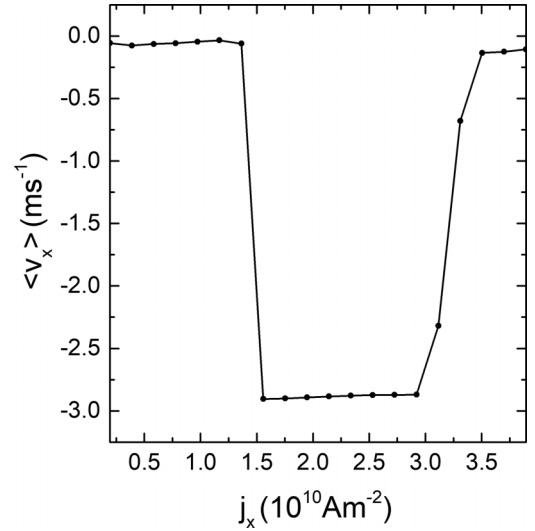

FIG. 2. $\langle v_x \rangle$ vs j_x for the system from Fig. 1 with x direction ac driving at $\omega = 5.57 \times 10^7$ Hz. For $j_x \leqslant 1.36 \times 10^{10}$ Am^{-2}, the skyrmion is in the pinned phase (PP), where the slight deviation of the velocity from zero is associated with transient motion that occurs before a stable localized orbit forms. The constant velocity phase (CVP) appears over the interval 1.5×10^{10} Am$^{-2} \leqslant j_x \leqslant 3.0 \times 10^{10}$ Am^{-2}, where $\langle v_x \rangle \approx -3$ ms^{-1}. Here the skyrmion moves in the negative x direction. For larger values of j_x, the system enters a reentrant pinning phase (RPP), where the velocities are significantly reduced but do not reach zero due to the transient motion.

a steady state. We normalize the simulation time units to $t = (\hbar/J)\tau$ and the current density units to $\mathbf{j} = (2eJ/\hbar a^2)\mathbf{j}'$, where τ and $\mathbf{j}'$ are the normalized time and current, respectively.

III. AC DRIVE ALONG THE x DIRECTION

We first consider ac driving applied along the x direction, so that $j_x \neq 0$ and $j_y = 0$. The ac drive frequency is $\omega = 5.57 \times 10^7$ Hz and j_x is in the range 0.19×10^{10} Am$^{-2} \leqslant j_x \leqslant 3.89 \times 10^{10}$ Am^{-2}, which is low enough that the skyrmion in the sample does not annihilate.

In Fig. 2 we plot the time-averaged skyrmion velocity $\langle v_x \rangle$ versus the ac amplitude j_x. When $j_x < 1.5 \times 10^{10}$ Am^{-2}, the average skyrmion velocity is nearly zero. This is the initial pinned phase (PP), and the slight deviation of the velocity from zero is produced by the brief initial period of time during which the skyrmion orbit adjusts to changes in the ac driving amplitude. A representative skyrmion trajectory showing this transient motion is illustrated in Fig. 3(a). As j_x increases, the skyrmion orbit increases in size and becomes more unstable. At $j_x = 1.36 \times 10^{10}$ Am^{-2}, the skyrmion velocity increases abruptly to $\langle v_x \rangle \approx -3$ ms^{-1}, indicating that a depinning threshold has been crossed. The net motion of the skyrmion along the $-x$ direction in this phase is associated with an orbit that is too large to be stabilized between the linear protrusions, and therefore evolves into a translating orbit that carries the skyrmion across the sample. For 1.5×10^{10} Am$^{-2} < j_x < 2.9 \times 10^{10}$ Am^{-2}, the skyrmion is in a constant velocity phase (CVP) with a translating orbit that gives $\langle v_x \rangle \approx -3$ ms^{-1}. The skyrmion flow in the $-x$
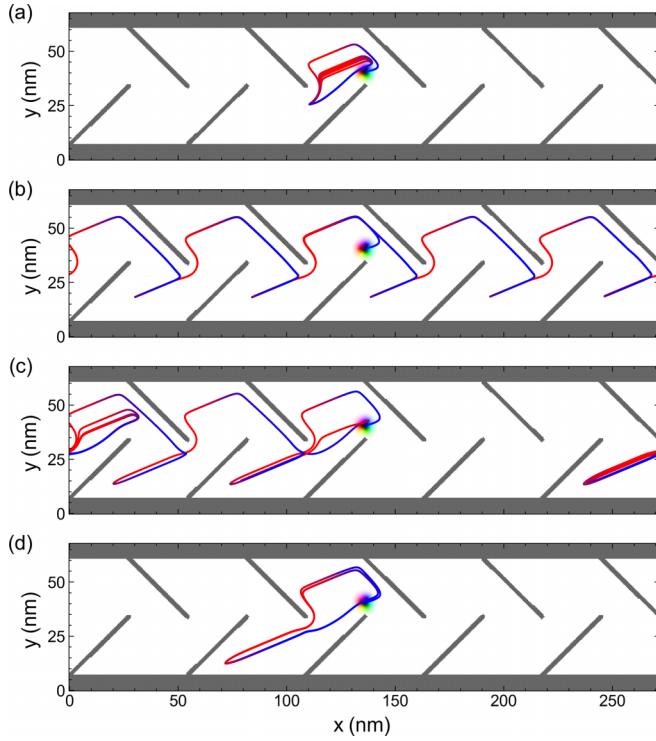
FIG. 3. Illustration of skyrmion trajectories for the system in Fig. 2, with x direction ac driving and $\omega = 5.57 \times 10^7$ Hz. The skyrmion trajectory color indicates the phase of the ac drive cycle as a gradient from positive x (blue) to negative x (red). (a) $j_x = 1.36 \times 10^{10}$ Am^{-2}, showing the transient motion in the pinned phase (PP). (b) $j_x = 2.53 \times 10^{10}$ Am^{-2}, where the skyrmion is transported with constant average velocity along $-x$. (c) $j_x = 3.31 \times 10^{10}$ Am^{-2}, corresponding to the transition between the constant velocity phase (CVP) and the reentrant pinning phase (RPP). (d) $j_x = 3.89 \times 10^{10}$ Am^{-2}, showing the RPP with a large stabilized orbit.

direction occurs along the hard substrate asymmetry direction, and the skyrmion must overcome the divots of the array in order to flow. The skyrmion trajectory in the CVP is shown in Fig. 3(b). The constant velocity is maintained even as j_x varies because the skyrmion translates by exactly one plaquette during each ac drive cycle, and the driving frequency is being held constant. For $j_x > 3.0 \times 10^{10}$ Am^{-2}, the system transitions to a reentrant pinning phase (RPP). The average skyrmion velocity in the RPP is again not exactly zero due to the transient adjustment of the orbit each time j_x is modified. As j_x increases, when the RPP arises a new stable localized orbit develops that is much more elongated than the orbit in the PP, as illustrated in Figs. 3(c) and 3(d). In the Supplemental Material [89], video3c.mp4 illustrates the skyrmion motion for Fig. 3(c). The portion of the orbit extending along the $-x$ direction becomes so extended that the skyrmion gets trapped underneath one of the linear defects and is no longer able to jump into a neighboring plaquette during the $-x$ portion of the ac drive cycle. This reentrant transition into a pinned state is not as sharp as the depinning transition found at lower j_x since the trapping process at high j_x is more gradual than the escape process at low j_x.

For ac driving along the x direction, we observe three distinctive phases with well-defined behavior. The CVP, where
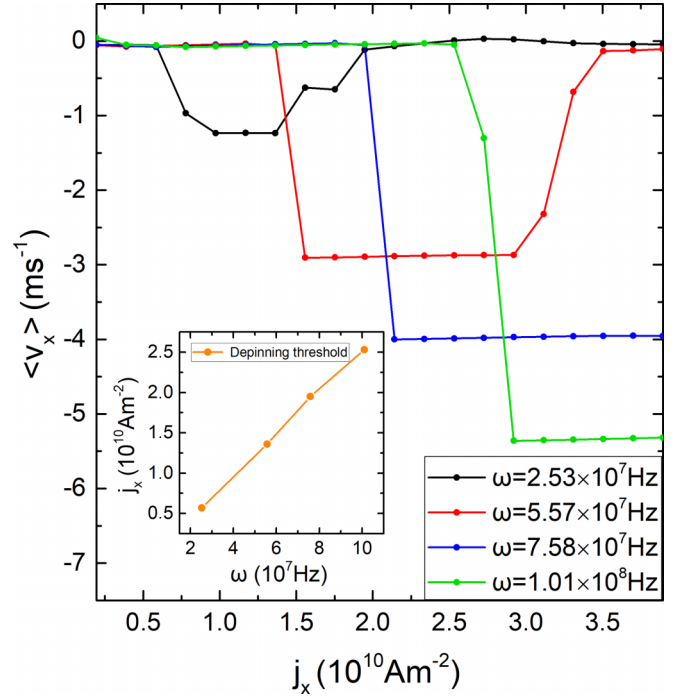
FIG. 4. $\langle v_x \rangle$ vs j_x for the system from Fig. 1 with ac driving applied along the x direction at different ac drive frequency values of $\omega = 2.53 \times 10^7$ Hz (black), $\omega = 5.57 \times 10^7$ Hz (red), $\omega = 7.58 \times 10^7$ Hz (blue), and $\omega = 1.01 \times 10^8$ Hz (green). The pinned phase (PP), constant velocity phase (CVP), and reentrant pinned phase (RPP) appear for $\omega \leqslant 5.57 \times 10^7$ Hz. For $\omega \geqslant 7.58 \times 10^7$ Hz the reentrant pinned phase does not occur over this range of j_x. Inset: The value of j_x at the depinning threshold marking the onset of the CVP vs ω.

the average skyrmion velocity is constant, can be useful for spintronic devices where precise control of the skyrmion motion is crucial. In addition, the skyrmion motion can be switched on or off by a fine adjustment in the external ac drive magnitude across the depinning transition. Although we performed simulations only for $j_x \leqslant 4 \times 10^{10}$ Am^{-2}, we expect that similar behavior will occur for larger values of j_x. In particular, as j_x increases, the size of the skyrmion orbit can continue to increase and may become unstable again, leading to the reemergence of a translating orbit.

A. Influence of the frequency ω

The motion described previously showed three distinctive phases at fixed ω, with well-defined ranges of j_x for each phase. We next investigate how the frequency ω of the ac drive affects the dynamics by varying it over the range 0.51×10^7 Hz $\leqslant \omega \leqslant 10.13 \times 10^7$ Hz and using the same range of j_x values from before.

In Fig. 4 we plot the average skyrmion velocity $\langle v_x \rangle$ versus j_x for different values of ω. The behavior is similar in each case. The PP appears for all values of ω simulated in this work. The CVP is also observed for all values of ω; however, the width of this phase is strongly affected by ω. As ω increases, the onset of the CVP shifts towards higher values of j_x, so that the range of the PP becomes larger. This is more easily visible in the inset of Fig. 4, where we plot the depinning threshold
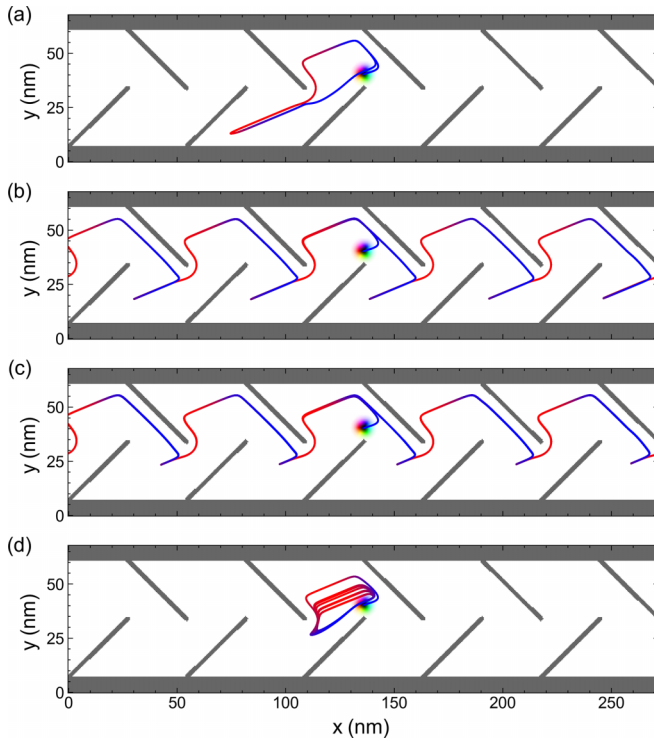
FIG. 5. Illustration of skyrmion trajectories for different values of ω with fixed $j_x = 2.53 \times 10^{10}$ Am^{-2} for the system in Fig. 4 with x-direction ac driving. The skyrmion trajectory color indicates the phase of the ac drive cycle as a gradient from positive x (blue) to negative x (red). (a) $\omega = 2.53 \times 10^7$ Hz, showing the reentrant pinned phase (RPP). (b) $\omega = 5.57 \times 10^7$ Hz, showing the constant velocity phase (CVP). (c) $\omega = 7.60 \times 10^7$ Hz in the CVP. (d) $\omega = 1.01 \times 10^8$ Hz, showing the pinned phase (PP).

versus ω and find a linear dependence. The increase in the depinning threshold occurs due to the oscillatory nature of the ac drive. As ω increases, the oscillations in the driving direction occur more rapidly, causing the skyrmion to experience a force in any given direction for a shorter period of time, and shrinking the skyrmion orbit accordingly. Thus, a larger current amplitude must be applied at higher ω in order to generate an orbit that is unstable enough to delocalize and produce net dc motion. Another interesting effect in Fig. 4 is the increase in the magnitude of the average skyrmion velocity in the CVP with increasing ω. Higher applied currents result in dc motion with enhanced velocities. Additionally, as ω increases, the CVP extends up to higher values of j_x. This is analogous to the increase of the depinning threshold as a function of ω; for higher ω values, larger values of j_x must be applied in order to obtain a skyrmion orbit that is large enough to reach the RPP. For the higher values of ω, $\omega \geqslant 7.58 \times 10^7$ Hz, the RPP is not observed over the range of j_x simulated here; however, we expect that the RPP would appear at even higher values of j_x.

Figure 5 illustrates the skyrmion trajectory at different values of ω. In Fig. 5(a) at $\omega = 2.53 \times 10^7$ Hz, the skyrmion is trapped in the RPP. As ω increases, the skyrmion orbit becomes narrower and extends less far along the x direction until the skyrmion no longer experiences confinement underneath a linear defect. When this occurs, the localized orbit destabilizes, permitting the CVP to appear with a translating
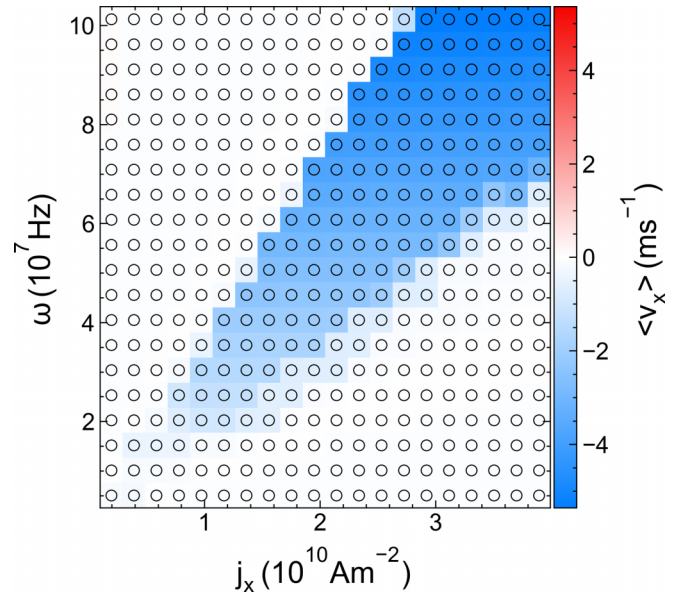

FIG. 6. Heat-map plot of $\langle v_x \rangle$ (color gradient) as a function of ω vs j_x for the system in Fig. 1 with x-direction ac driving. In the blue regions skyrmion transport occurs along the negative x direction, while in white regions the skyrmion is pinned. The circles indicate the discrete parameters used for the simulations.

orbit as shown in Fig. 5(b) for $\omega = 5.57 \times 10^7$ Hz. In Fig. 5(c) at $\omega = 7.60 \times 10^7$ Hz, the skyrmion is still in the CVP, but due to the increased ac frequency, the dead-end portion of the orbit extending in the $-x$ direction becomes less pronounced. When $\omega = 1.01 \times 10^8$ Hz, the frequency is so high that the orbit is no longer wide enough for the skyrmion to slip past the linear defect into the next plaquette, and the PP emerges, as shown in Fig. 5(d) and video5d.mp4 in the Supplemental Material.

B. Conditions for skyrmion transport with ac drive along the x direction

Now that we understand the individual effects of both ac drive magnitude, j_x, and the ac drive frequency, ω, for ac driving in the x direction, we perform a series of simulations in which we vary both parameters and identify the optimal conditions for skyrmion transport. In Fig. 6 we plot a heat map of the skyrmion average velocity $\langle v_x \rangle$ as a function of ω versus j_x. Both the PP and RPP appear as white regions since both of these phases have very low average velocities. They are separated by the blue region, which represents the CVP. For values of ω and j_x falling above the blue region, the system is in the PP, where the skyrmion exhibits no net motion and the trajectories are very similar to those shown in Fig. 5(d) and Fig. 3(a). For ω and j_x values that are below the blue region, the system is in the RPP, where the skyrmion has no net motion and the trajectory is similar to those shown in Fig. 5(a) and Fig. 3(d). In the CVP phase, the skyrmion trajectories are similar to those shown in Figs. 5(b), 5(c) and Fig. 3(b). The speed at which the skyrmion is transported along the sample in the CVP is governed by ω. Note that as ω increases, the blue region becomes darker, indicating higher velocity magnitudes. Additionally, the onset of skyrmion transport and the range of j_x values for which it occurs also change as ω varies.
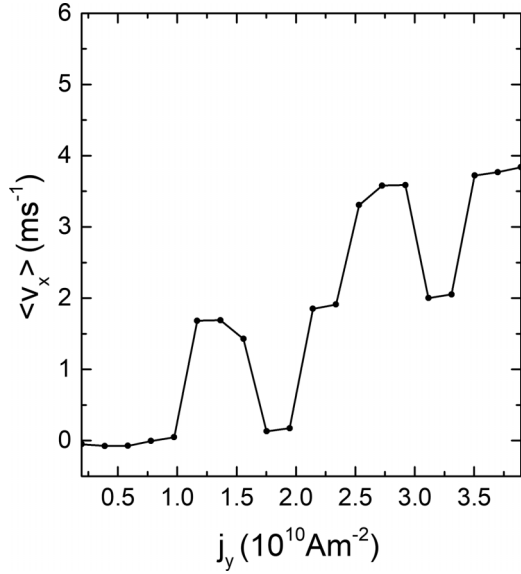
FIG. 7. $\langle v_x \rangle$ vs j_y with fixed $\omega = 3.55 \times 10^7$ Hz for the system shown in Fig. 1 with ac driving along the y direction. Here the skyrmion moves in the positive x direction.

Figure 6 can be very useful for the design of a device using a linear protrusion array of defects, since it clearly shows the necessary parameters for skyrmion transport through the sample. In addition, it indicates how rapidly the skyrmion can be transported in the CVP. In our simulations, the skyrmion is always stable and we did not observe any annihilation effects, which is crucial for technological applications where skyrmions are to be used as information carriers. The skyrmion may deform when the ac drive pushes it against the magnetic walls, but the deformation does not significantly impact the skyrmion dynamics, as shown in the videos from the Supplemental Material. We expect, however, that if a much stronger ac drive amplitude is applied, the skyrmion may strongly deform and be annihilated when it comes into contact with the linear protrusion magnetic walls.

IV. AC DRIVE ALONG THE y DIRECTION

In Sec. III we showed that applying the ac drive along the x direction may induce skyrmion transport in the $-x$ direction. Here, we investigate the same system from Fig. 1 but apply the ac drive along the y direction, giving $j_x = 0$ and $j_y \neq 0$.

In Fig. 7 we plot the skyrmion average velocity $\langle v_x \rangle$ as a function of the ac drive amplitude j_y for fixed $\omega = 3.55 \times 10^7$ Hz. We find several different dynamic regimes that we can classify as a pinned phase (PP), a reentrant pinned phase (RPP), and different types of constant velocity phases (CVPs). For $j_y \lesssim 0.97 \times 10^{10}$ Am^{-2}, the skyrmion exhibits no net motion and is in the PP as illustrated in Fig. 8(a). As was the case for $j_x \neq 0$ driving, we find that the velocities are not exactly zero since the skyrmion undergoes transient motion before the localized orbit becomes stabilized. In the interval 1.75×10^{10} Am$^{-2} \leqslant j_y \leqslant 2.34 \times 10^{10}$ Am^{-2}, the skyrmion orbit is unstable and the dc velocity takes the value $\langle v_x \rangle \approx 1.68$ ms^{-1}, indicating that the skyrmion is in the CVP illustrated in Fig. 8(b). Here the skyrmion translates by one plaquette during every ac drive cycle. The skyrmion
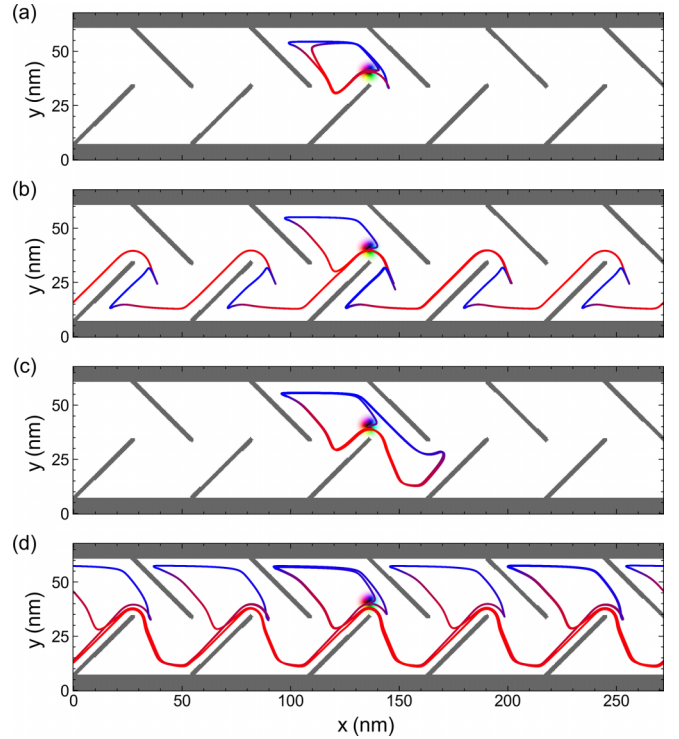

FIG. 8. Illustration of skyrmion trajectories for the system in Fig. 1 under y-direction ac driving with fixed $\omega = 3.55 \times 10^7$ Hz. The skyrmion trajectory color indicates the phase of the ac drive cycle as a gradient from positive y (blue) to negative y (red). (a) $j_y = 0.97 \times 10^{10}$ Am^{-2} in the pinned phase (PP), where the skyrmion is in a closed localized orbit. (b) $j_y = 1.36 \times 10^{10}$ Am^{-2} in the constant velocity phase (CVP), where the skyrmion translates at $\langle v_x \rangle \approx 1.68$ ms^{-1} and moves one plaquette during every ac drive cycle. (c) $j_y = 1.95 \times 10^{10}$ Am^{-2} in the reentrant pinned phase (RPP), where the skyrmion enters a stable localized orbit and the net dc motion drops to zero. (d) $j_y = 3.69 \times 10^{10}$ Am^{-2} in a second CVP, where the skyrmion translates at $\langle v_x \rangle \approx 3.8$ ms^{-1} and moves two plaquettes during every ac drive cycle.

has a greater interaction with the lower part of the sample when the ac driving is in the y direction due to the skyrmion Hall angle effect, and the net transport is in the positive x direction, unlike the case of x direction ac driving, which produced dc motion in the negative x direction. Above $j_y = 1.36 \times 10^{10}$ Am^{-2}, the skyrmion average velocity drops to a value that is very close to zero. In this region, a localized skyrmion orbit becomes stable again and the dc motion is lost, giving a RPP as shown in Fig. 8(c). Here the width of the skyrmion orbit matches the spacing between the linear protrusions. When $j_y = 1.94 \times 10^{10}$ Am^{-2}, the localized orbit destabilizes because it is now too wide to fit inside a single plaquette, and dc motion reappears. Notice that the skyrmion is now translating by two plaquettes during every dc drive cycle. A blue orbit appears in the top portion of every plaquette only because the total number of plaquettes is odd. Figure 7 shows that the skyrmion velocity for the state in Fig. 8(d) is twice as large as that in Fig. 8(b). For larger values of j_y, the skyrmion dynamics oscillate among a series of CVPs where the velocity locks to a constant value that differs from one CVP to the next and is determined
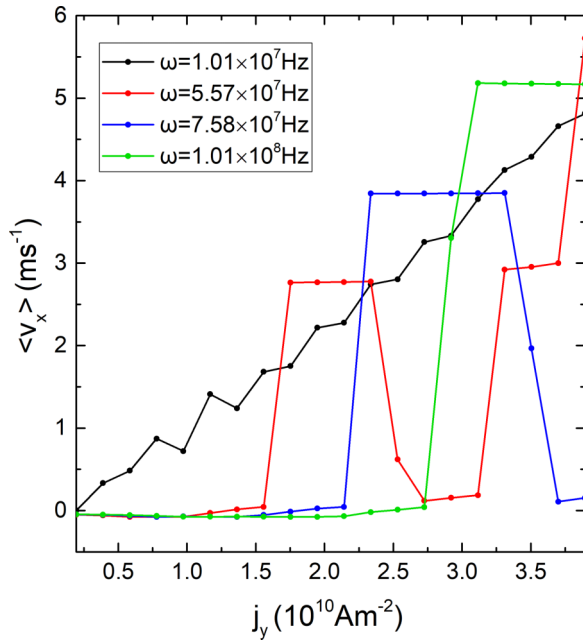
FIG. 9. $\langle v_x \rangle$ vs j_y for the system from Fig. 7 with ac driving along the y direction at $\omega = 1.01 \times 10^7$ Hz (black), $\omega = 5.57 \times 10^7$ Hz (red), $\omega = 7.58 \times 10^7$ Hz (blue), and $\omega = 1.01 \times 10^8$ Hz (green).

FIG. 10. Illustration of skyrmion trajectories for the system in Fig. 9 under y-direction ac driving with fixed $j_y = 3.12 \times 10^{10}$ Am^{-2}. The skyrmion trajectory color indicates the phase of the ac drive cycle as a gradient from positive y (blue) to negative y (red). (a) $\omega = 1.01 \times 10^7$ Hz. (b) $\omega = 5.57 \times 10^7$ Hz. (c) $\omega = 7.58 \times 10^7$ Hz. (d) $\omega = 1.01 \times 10^8$ Hz.

by the number of plaquettes the skyrmion can translate in each ac drive cycle. In every CVP, the skyrmion follows a distinct delocalized orbit as it translates through the sample. Figure 8(d) shows an example of the skyrmion trajectory in the CVP at $j_y = 3.69 \times 10^{10}$ Am^{-2}. This trajectory is also illustrated in video8d.mp4 in the Supplemental Material. The fact that the skyrmion translates along the easy direction of the substrate asymmetry for y-direction driving makes it possible for the skyrmion to move through multiple plaquettes per ac drive cycle, giving multiple CVP states. This is in contrast to the single CVP state found for x-direction driving, when the motion is along the hard direction of the substrate asymmetry and the translating orbit is confined by the substrate in such a way that the skyrmion can travel only exactly one plaquette during each ac drive cycle.

A. Influence of the frequency ω

We next consider how the ac driving frequency ω affects the dynamics under y-direction driving by varying ω over the range 0.51×10^7 Hz $\leqslant \omega \leqslant 10.13 \times 10^7$ Hz. In Fig. 9 we plot the average skyrmion velocity $\langle v_x \rangle$ versus j_y for selected values of ω. When $\omega = 1.01 \times 10^7$ Hz, the CVP and RPP vanish. As low values of ω such as this one, the skyrmion can coast along the bottom of the array over a distance of many plaquettes during the $-y$ portion of the ac drive cycle, as shown in Fig. 10(a) at $j_y = 3.12 \times 10^{10}$ Am^{-2}. The Magnus term rotates the repulsive force from the protrusions and walls into a $+x$ velocity, resulting in a Magnus velocity boost effect. The confined excursion into the upper portion of the sample provides only a small perturbation to the boosted $+x$ velocity and is insufficient to quantize the velocity values. As a result, $\langle v_x \rangle$ increases almost linearly with the ac drive amplitude j_y. For $\omega = 5.57 \times 10^7$ Hz, $\omega = 7.58 \times 10^7$ Hz,
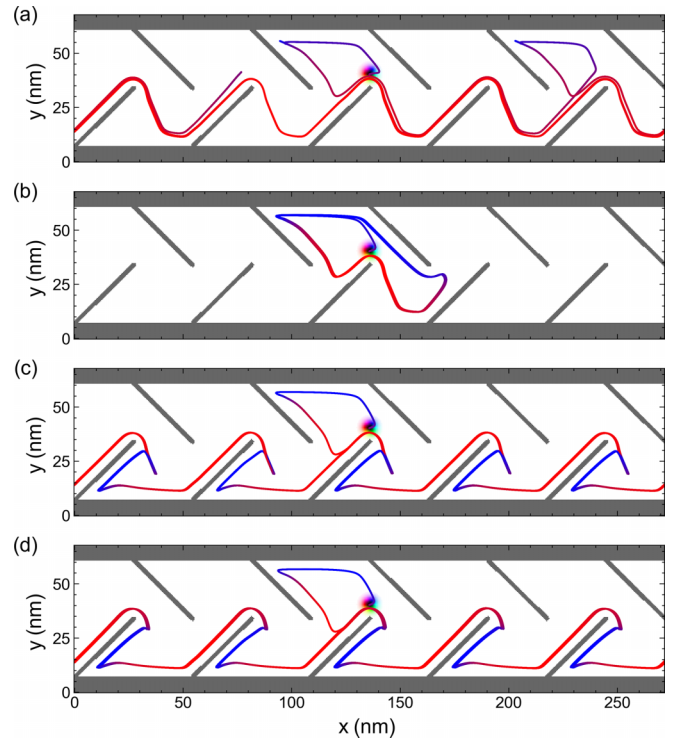
and $\omega = 1.01 \times 10^8$ Hz, the behavior is similar to what was observed in Fig. 7, with the CVP and RPP both present but extending over a wider range of j_y values compared to the system with $\omega = 3.55 \times 10^7$ Hz. For $\omega = 5.57 \times 10^7$ Hz the skyrmion becomes trapped in a RPP, as illustrated in Fig. 10(b) at $j_y = 3.12 \times 10^{10}$ Am^{-2}. Here the size of the skyrmion orbit matches the length scale of the plaquette. For $\omega = 7.58 \times 10^7$ Hz at the same value of j_y, the orbit is delocalized again and the skyrmion flows along the positive x direction as shown in Fig. 10(c). In the Supplemental Material, video10c.mp4 shows the skyrmion trajectory in detail. Figure 9 indicates that the skyrmion average velocity in each CVP becomes larger for higher frequencies, as illustrated in Fig. 10(d) where we show another type of CVP with higher average velocity at $\omega = 1.01 \times 10^8$ Hz. The velocity increase is simply due to the higher ac driving frequency; the skyrmion still translates by one plaquette per ac drive cycle but the drive cycle is shorter at higher ω, so the skyrmion moves faster. The onset of the CVP in Fig. 9 shifts to higher j_y with increasing ω because at high ac driving frequencies, the skyrmion orbits become narrower and so larger values of j_y must be applied to destabilize the localized orbits.

B. Conditions for skyrmion transport with ac drive along the y direction

In Fig. 11 we plot a heatmap of the skyrmion average velocity $\langle v_x \rangle$ as a function of the frequency ω versus the drive
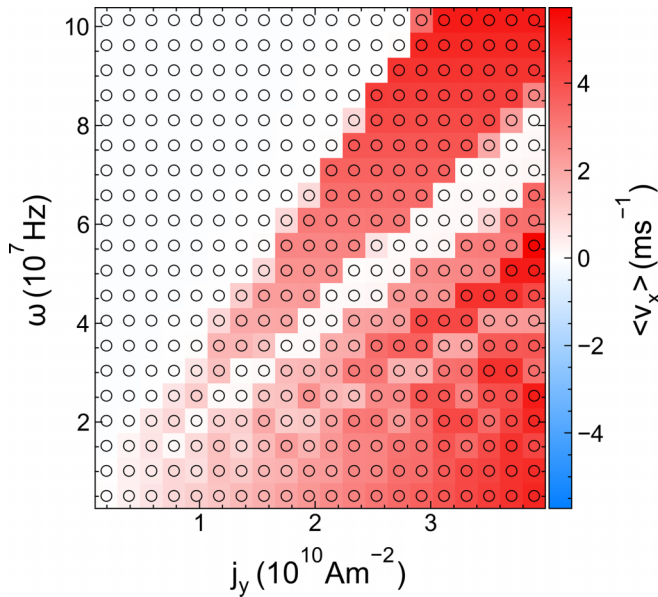
FIG. 11. Heat-map plot of $\langle v_x \rangle$ (color gradient) as a function of ω vs j_y for the system in Fig. 1 with y-direction ac driving. In the red regions skyrmion transport occurs along the positive x direction, while in white regions the skyrmion is pinned. The circles indicate the discrete parameters used for the simulations.

magnitude j_y. There are two large red regions corresponding to the dynamic phases where the skyrmion is being transported. The white regions correspond to phases where the skyrmion exhibits no net motion. The first white region that occurs for lower values of j_y is the PP where the localized skyrmion orbit is stabilized with no net motion. At slightly larger values of j_y we find the first red region, corresponding to the CVP in which the localized skyrmion orbit is unstable and the skyrmion translates through the sample along the positive x direction. In this phase, as ω increases, the range of j_y where the CVP is stable increases, and the average skyrmion velocity also increases in a manner analogous to that discussed for Fig. 6. The second white region, located between two red regions, is the RPP, where the increase in j_y stabilizes the previously unstable localized skyrmion orbit, resulting in a state with $\langle v_x \rangle = 0$. In addition, as ω increases, the RPP expands over a wider range of j_y. The second red region that occurs for larger values of j_y corresponds to a mixture of CVP and a skyrmion transport phase in which the velocity increases almost linearly with j_y. In this region, for larger values of j_y the system is in a clearly defined CVP phase where multiple constant velocity states can be accessed by varying the ac drive amplitude. As ω is reduced, the CVP is lost and the skyrmion velocity increases linearly with j_y. This is a result of the velocity boost effect from the Magnus term, which makes the motion during the $+y$ and $-y$ portions of the ac drive cycle very asymmetric and destroys the velocity quantization found for larger values of ω.

As we have seen, when the ac drive is applied along the x direction, the skyrmion flows along $-x$, the hard substrate asymmetry direction, while when the ac drive is applied along the y direction, the skyrmion instead flows along $+x$, the easy substrate asymmetry direction. The plots in Figs. 6 and 11

show in great detail the possibilities for achieving controlled skyrmion motion by tuning the values of ω and either j_x or j_y. We note that for the parameters we consider, no annihilation effects were observed; however, for sufficiently large ac drive amplitudes, we expect that the skyrmion would be pushed hard enough against the walls and linear protrusions that annihilation events would occur. Thus there is a finite range of ac driving where control of stable skyrmion motion can be achieved.

V. SUMMARY

Using an atomistic model for simulating individual atomic magnetic moments, we investigated the dynamical behavior of a single skyrmion interacting with a linear protrusion array of defects with ac driving applied along either the x or y directions in the absence of thermal effects. When the ac driving is parallel to the x direction, the skyrmion can be transported along the negative x or hard substrate asymmetry direction over a range of ac drive amplitudes. There are three distinct phases of motion. At low ac amplitudes, the skyrmion enters a stable localized orbit and has no net dc motion, giving a pinned phase. When the ac amplitude increases, the localized skyrmion orbit expands in size and becomes unstable, leading to the emergence of a constant velocity phase in which the skyrmion follows a translating orbit along the negative x direction. As the ac driving amplitude becomes even larger, the skyrmion orbit continues to grow until a localized orbit restabilizes again due to confinement by the linear protrusions, resulting in a reentrant pinned phase with no net dc transport. When the ac drive frequency increases, we find that the range of ac drive amplitudes over which each phase is stable increases, and that the skyrmion average velocity in the constant velocity phase also increases.

When the ac drive is applied along the y direction, the skyrmion can be transported along the positive x or easy flow direction of the substrate asymmetry for a range of ac amplitudes. The velocity boost effect produced by the Magnus term for y-direction driving in the presence of the substrate permits a greater range of translating orbits to appear, and we observe a richer dynamical response compared to driving along the x direction. At low values of ac drive amplitudes, the skyrmion orbit is localized and we find a pinned phase with no net motion. As the ac amplitude increases, the localized orbit destabilizes and the skyrmion enters a constant velocity phase in which it translates along the positive x direction with constant velocity. Further increases in the ac drive amplitude restabilize a localized orbit, resulting in the emergence of a reentrant pinned phase with no net motion. For sufficiently high values of the ac drive amplitude, the skyrmion orbit becomes too large to localize, and we find a series of distinct constant velocity phases, each of which has a different average velocity value determined by the number of plaquettes the skyrmion traverses during each ac drive cycle. Just as in the case for x-direction ac driving, increasing the ac driving frequency for y-direction ac driving causes each phase to extend over a wider range of ac drive amplitudes and also increases the average velocity in the constant velocity phase. Above the reentrant pinning phase, the constant velocity phases become more stable as the ac frequency increases,

while for small frequencies these phases disappear completely and are replaced by a regime in which the average skyrmion velocity increases linearly with increasing ac drive amplitude. It is worth mentioning that our analysis did not account for thermal fluctuations and nonadiabatic effects in the spin current. It is known that temperature effects can alter the skyrmion stabilization [91], induce initial creep motion, and change the transition points [92]. Additionally, nonadiabatic contributions within the spin current can change the skyrmion Hall angle [36]. The inclusion of these factors could introduce modifications to the observed results and can be an interesting consideration for future works. Furthermore, exploring the scenario of an ac drive aligned with the angles of the linear protrusions could produce strong ratchet effects. This aspect remains unexplored in our current study and presents an interesting direction for future research.

Our findings can be useful for realizing novel spintronic devices where controlled skyrmion motion is crucial. In our system, the ability to control the direction and velocity of the skyrmion motion makes it possible to efficiently transport information in a device where the skyrmion serves as an information carrier. The level of skyrmion control that we obtain in our sample is similar to the control achieved in Ref. [53], where the skyrmion is also controlled precisely using ac currents. The key difference from the previous work is that in the linear protrusion device considered here, the skyrmion average velocities are similar for transport in both the positive and negative x directions, resulting in a more energy-efficiency skyrmion transport overall.

[1] C. Negru, F. Pop, V. Cristea, N. Bessisy, and J. Li, Energy efficient cloud storage service: Key issues and challenges, in *2013 Fourth International Conference on Emerging Intelligent Data and Web Technologies, Xi'an, China* (IEEE, Piscataway, NJ, 2013), pp. 763–766.

[2] N. Nagaosa and Y. Tokura, Topological properties and dynamics of magnetic skyrmions, Nat. Nanotechnol. **8**, 899 (2013).

[3] S.-G. Je, H.-S. Han, S. K. Kim, S. A. Montoya, W. Chao, I.-S. Hong, E. E. Fullerton, K.-S. Lee, K.-J. Lee, M.-Y. Im, and J.-I. Hong, Direct demonstration of topological stability of magnetic skyrmions *via* topology manipulation, ACS Nano **14**, 3251 (2020).

[4] X. S. Wang, H. Y. Yuan, and X. R. Wang, A theory on skyrmion size, Commun. Phys. **1**, 31 (2018).

[5] S. Mühlbauer, B. Binz, F. Jonietz, C. Pfleiderer, A. Rosch, A. Neubauer, R. Georgii, and P. Böni, Skyrmion lattice in a chiral magnet, Science **323**, 915 (2009).

[6] X. Z. Yu, Y. Onose, N. Kanazawa, J. H. Park, J. H. Han, Y. Matsui, N. Nagaosa, and Y. Tokura, Real-space observation of a two-dimensional skyrmion crystal, Nature (London) **465**, 901 (2010).

[7] C. Pfleiderer, T. Adams, A. Bauer, W. Biberacher, B. Binz, F. Birkelbach, P. Böni, C. Franz, R. Georgii, M. Janoschek, F. Jonietz, T. Keller, R. Ritz, S. Mühlbauer, W. Münzer, A. Neubauer, B. Pedersen, and A. Rosch, Skyrmion lattices in metallic and semiconducting B20 transition metal compounds, J. Phys.: Condens. Matter **22**, 164207 (2010).

[8] W. Münzer, A. Neubauer, T. Adams, S. Mühlbauer, C. Franz, F. Jonietz, R. Georgii, P. Böni, B. Pedersen, M. Schmidt, A. Rosch, and C. Pfleiderer, Skyrmion lattice in the doped semiconductor $Fe_{1-x}Co_x$ Si, Phys. Rev. B **81**, 041203(R) (2010).

[9] K. Everschor-Sitte, J. Masell, R. M. Reeve, and M. Kläui, Perspective: Magnetic skyrmions-Overview of recent progress in an active research field, J. Appl. Phys. **124**, 240901 (2018).

[10] A. Fert, V. Cros, and J. Sampaio, Skyrmions on the track, Nat. Nanotechnol. **8**, 152 (2013).

[11] A. Fert, N. Reyren, and V. Cros, Magnetic skyrmions: advances in physics and potential applications, Nat. Rev. Mater. **2**, 17031 (2017).

[12] T. Schulz, R. Ritz, A. Bauer, M. Halder, M. Wagner, C. Franz, C. Pfleiderer, K. Everschor, M. Garst, and A. Rosch, Emergent electrodynamics of skyrmions in a chiral magnet, Nat. Phys. **8**, 301 (2012).

[13] F. Jonietz, S. Mühlbauer, C. Pfleiderer, A. Neubauer, W. Münzer, A. Bauer, T. Adams, R. Georgii, P. Böni, R. A. Duine, K. Everschor, M. Garst, and A. Rosch, Spin transfer torques in MnSi at ultralow current densities, Science **330**, 1648 (2010).

[14] S. Luo and L. You, Skyrmion devices for memory and logic applications, APL Mater. **9**, 050901 (2021).

[15] Y. Shu, Q. Li, J. Xia, P. Lai, Z. Hou, Y. Zhao, D. Zhang, Y. Zhou, X. Liu, and G. Zhao, Realization of the skyrmionic logic gates and diodes in the same racetrack with enhanced and modified edges, Appl. Phys. Lett. **121**, 042402 (2022).

[16] X. Zhang, M. Ezawa, and Y. Zhou, Magnetic skyrmion logic gates: conversion, duplication and merging of skyrmions, Sci. Rep. **5**, 9400 (2015).

[17] J. C. Bellizotti Souza, N. Vizarim, C. J. O. Reichhardt, C. Reichhardt, and P. A. Venegas, Magnus induced diode effect for skyrmions in channels with periodic potentials, J. Phys.: Condens. Matter **35**, 015804 (2022).

[18] Y. Feng, X. Zhang, G. Zhao, and G. Xiang, A skyrmion diode based on skyrmion Hall effect, IEEE Trans. Elect. Dev. **69**, 1293 (2022).

[19] J. Wang, J. Xia, X. Zhang, X. Zheng, G. Li, L. Chen, Y. Zhou, J. Wu, H. Yin, R. Chantrell, and Y. Xu, Magnetic skyrmionium diode with a magnetic anisotropy voltage gating, Appl. Phys. Lett. **117**, 202401 (2020).

[20] K. M. Song, J.-S. Jeong, B. Pan, X. Zhang, J. Xia, S. Cha, T.-E. Park, K. Kim, S. Finizio, J. Raabe, J. Chang, Y. Zhou, W. Zhao, W. Kang, H. Ju, and S. Woo, Skyrmion-based artificial synapses for neuromorphic computing, Nat. Electron. **3**, 148 (2020).

[21] D.-H. Jung, H.-S. Han, N. Kim, G. Kim, S. Jeong, S. Lee, M. Kang, M.-Y. Im, and K.-S. Lee, Magnetic skyrmion diode: Uni-directional skyrmion motion via symmetry breaking of potential energy barriers, Phys. Rev. B **104**, L060408 (2021).

[22] L. Zhao, X. Liang, J. Xia, G. Zhao, and Y. Zhou, A ferromag-netic skyrmion-based diode with a voltage-controlled potential barrier, Nanoscale **12**, 9507 (2020).

[23] X. Zhang, Y. Zhou, M. Ezawa, G. P. Zhao, and W. Zhao, Mag-netic skyrmion transistor: skyrmion motion in a voltage-gated nanotrack, Sci. Rep. **5**, 11369 (2015).

[24] R. Msiska, J. Love, J. Mulkers, J. Leliaert, and K. Everschor-Sitte, Audio classification with skyrmion reservoirs, Adv. Intell. Syst. **5**, 2200388 (2023).

[25] S. Li, W. Kang, Y. Huang, X. Zhang, Y. Zhou, and W. Zhao, Magnetic skyrmion-based artificial neuron device, Nanotechnology **28**, 31LT01 (2017).

[26] S. Li, W. Kang, X. Zhang, T. Nie, Y. Zhou, K. L. Wang, and W. Zhao, Magnetic skyrmions for unconventional computing, Mater. Horiz. **8**, 854 (2021).

[27] S. Luo, M. Song, X. Li, Y. Zhang, J. Hong, X. Yang, X. Zou, N. Xu, and L. You, Reconfigurable skyrmion logic gates, Nano Lett. **18**, 1180 (2018).

[28] X. Zhang, J. Xia, O. A. Tretiakov, M. Ezawa, G. Zhao, Y. Zhou, X. Liu, and M. Mochizuki, Laminar and transiently disordered dynamics of magnetic-skyrmion pipe flow, Phys. Rev. B **108**, 144428 (2023).

[29] C. Pfleiderer, Surfaces get hairy, Nat. Phys. **7**, 673 (2011).

[30] R. Wiesendanger, Nanoscale magnetic skyrmions in metallic films and multilayers: a new twist for spintronics, Nat. Rev. Mater. **1**, 16044 (2016).

[31] W. Kang, Y. Huang, X. Zhang, Y. Zhou, and W. Zhao, Skyrmion-electronics: An overview and outlook, Proc. IEEE **104**, 2040 (2016).

[32] X. Zhang, Y. Zhou, K. M. Song, T.-E. Park, J. Xia, M. Ezawa, X. Liu, W. Zhao, G. Zhao, and S. Woo, Skyrmion-electronics: Writing, deleting, reading and processing magnetic skyrmions toward spintronic applications, J. Phys.: Condens. Matter **32**, 143001 (2020).

[33] C. J. O. Reichhardt, S. Z. Lin, D. Ray, and C. Reichhardt, Comparing the dynamics of skyrmions and superconducting vortices, Physica C **503**, 52 (2014).

[34] C. Reichhardt and C. J. O. Reichhardt, Depinning and nonequi-librium dynamic phases of particle assemblies driven over random and ordered substrates: a review, Rep. Prog. Phys. **80**, 026501 (2017).

[35] K. Litzius, I. Lemesh, B. Krüger, P. Bassirian, L. Caretta, K. Richter, F. Büttner, K. Sato, O. A. Tretiakov, J. Förster, R. M. Reeve, M. Weigand, I. Bykova, H. Stoll, G. Schütz, G. S. D. Beach, and M. Kläui, Skyrmion Hall effect revealed by direct time-resolved x-ray microscopy, Nat. Phys. **13**, 170 (2017).

[36] J. Iwasaki, M. Mochizuki, and N. Nagaosa, Universal current-velocity relation of skyrmion motion in chiral magnets, Nat. Commun. **4**, 1463 (2013).

[37] W. Jiang, X. Zhang, G. Yu, W. Zhang, X. Wang, M. B. Jungfleisch, J. E. Pearson, X. Cheng, O. Heinonen, K. L. Wang, Y. Zhou, A. Hoffmann, and S. G. E. te Velthuis, Direct observa-tion of the skyrmion Hall effect, Nat. Phys. **13**, 162 (2017).

[38] S.-Z. Lin, C. Reichhardt, C. D. Batista, and A. Saxena, Driven skyrmions and dynamical transitions in chiral magnets, Phys. Rev. Lett. **110**, 207202 (2013).

[39] S.-Z. Lin, C. Reichhardt, C. D. Batista, and A. Saxena, Particle model for skyrmions in metallic chiral magnets: Dynamics, pinning, and creep, Phys. Rev. B **87**, 214419 (2013).

[40] K. Zeissler, S. Finizio, C. Barton, A. J. Huxtable, J. Massey, J. Raabe, A. V. Sadovnikov, S. A. Nikitov, R. Brearton, T. Hesjedal, G. van der Laan, M. C. Rosamond, E. H. Linfield, G. Burnell, and C. H. Marrows, Diameter-independent skyrmion Hall angle observed in chiral magnetic multilayers, Nat. Commun. **11**, 428 (2020).

[41] C. Reichhardt, D. Ray, and C. J. O. Reichhardt, Quantized transport for a skyrmion moving on a two-dimensional periodic substrate, Phys. Rev. B **91**, 104426 (2015).

[42] C. Reichhardt, D. Ray, and C. J. O. Reichhardt, Nonequilib-rium phases and segregation for skyrmions on periodic pinning arrays, Phys. Rev. B **98**, 134418 (2018).

[43] J. Feilhauer, S. Saha, J. Tobik, M. Zelent, L. J. Heyderman, and M. Mruczkiewicz, Controlled motion of skyrmions in a magnetic antidot lattice, Phys. Rev. B **102**, 184425 (2020).

[44] N. P. Vizarim, J. C. B. Souza, C. Reichhardt, C. J. O. Reichhardt, and P. A. Venegas, Directional locking and the in-fluence of obstacle density on skyrmion dynamics in triangular and honeycomb arrays, J. Phys.: Condens. Matter **33**, 305801 (2021).

[45] N. P. Vizarim, C. Reichhardt, C. J. O. Reichhardt, and P. A. Venegas, Skyrmion dynamics and topological sorting on peri-odic obstacle arrays, New J. Phys. **22**, 053025 (2020).

[46] C. Reichhardt and C. J. O. Reichhardt, Commensuration ef-fects on skyrmion Hall angle and drag for manipulation of skyrmions on two-dimensional periodic substrates, Phys. Rev. B **105**, 214437 (2022).

[47] V. L. Carvalho-Santos, M. A. Castro, D. Salazar-Aravena, D. Laroze, R. M. Corona, S. Allende, and D. Altbir, Skyrmion propagation along curved racetracks, Appl. Phys. Lett. **118**, 172407 (2021).

[48] A. Korniienko, A. Kákay, D. D. Sheka, and V. P. Kravchuk, Effect of curvature on the eigenstates of magnetic skyrmions, Phys. Rev. B **102**, 014432 (2020).

[49] K. V. Yershov, A. Kákay, and V. P. Kravchuk, Curvature-induced drift and deformation of magnetic skyrmions: Com-parison of the ferromagnetic and antiferromagnetic cases, Phys. Rev. B **105**, 054425 (2022).

[50] N. P. Vizarim, C. Reichhardt, P. A. Venegas, and C. J. O. Reichhardt, Guided skyrmion motion along pinning array in-terfaces, J. Magn. Magn. Mater. **528**, 167710 (2021).

[51] C.-L. Zhang, J.-N. Wang, C.-K. Song, N. Mehmood, Z.-Z. Zeng, Y.-X. Ma, J.-B. Wang, and Q.-F. Liu, Edge-guided heart-shaped skyrmion, Rare Metals **41**, 865 (2022).

[52] C. Reichhardt, D. Ray, and C. J. O. Reichhardt, Magnus-induced ratchet effects for skyrmions interacting with asymmet-ric substrates, New J. Phys. **17**, 073034 (2015).

[53] J. C. B. Souza, N. P. Vizarim, C. J. O. Reichhardt, C. Reichhardt, and P. A. Venegas, Skyrmion ratchet in funnel geometries, Phys. Rev. B **104**, 054434 (2021).

[54] W. Chen, L. Liu, Y. Ji, and Y. Zheng, Skyrmion ratchet effect driven by a biharmonic force, Phys. Rev. B **99**, 064431 (2019).

[55] B. Göbel and I. Mertig, Skyrmion ratchet propagation: utilizing the skyrmion Hall effect in AC racetrack storage devices, Sci. Rep. **11**, 3020 (2021).

[56] R. Yanes, F. Garcia-Sanchez, R. F. Luis, E. Martinez, V. Raposo, L. Torres, and L. Lopez-Diaz, Skyrmion motion induced by voltage-controlled in-plane strain gradients, Appl. Phys. Lett. **115**, 132401 (2019).

[57] S. L. Zhang, W. W. Wang, D. M. Burn, H. Peng, H. Berger, A. Bauer, C. Pfleiderer, G. van der Laan, and T. Hesjedal, Manipulation of skyrmion motion by magnetic field gradients, Nat. Commun. **9**, 2115 (2018).

[58] K. Everschor, M. Garst, B. Binz, F. Jonietz, S. Mühlbauer, C. Pfleiderer, and A. Rosch, Rotating skyrmion lattices by spin torques and field or temperature gradients, Phys. Rev. B **86**, 054432 (2012).

[59] L. Kong and J. Zang, Dynamics of an insulating skyrmion under a temperature gradient, Phys. Rev. Lett. **111**, 067203 (2013).

[60] X. Gong, H. Y. Yuan, and X. R. Wang, Current-driven skyrmion motion in granular films, Phys. Rev. B **101**, 064421 (2020).

[61] H. Y. Yuan, X. S. Wang, M.-H. Yung, and X. R. Wang, Wiggling skyrmion propagation under parametric pumping, Phys. Rev. B **99**, 014428 (2019).

[62] R. M. Menezes, J. F. S. Neto, C. C. de Souza Silva, and M. V. Milošević, Manipulation of magnetic skyrmions by superconducting vortices in ferromagnet-superconductor heterostructures, Phys. Rev. B **100**, 014431 (2019).

[63] J. F. Neto and C. C. de Souza Silva, Mesoscale phase separation of skyrmion-vortex matter in chiral-magnet–superconductor heterostructures, Phys. Rev. Lett. **128**, 057001 (2022).

[64] X. Zhang, J. Xia, and X. Liu, Structural transition of skyrmion quasiparticles under compression, Phys. Rev. B **105**, 184402 (2022).

[65] J. C. Bellizotti Souza, N. P. Vizarim, C. J. O. Reichhardt, C. Reichhardt, and P. A. Venegas, Spontaneous skyrmion conformal lattice and transverse motion during dc and ac compression, New J. Phys. **25**, 053020 (2023).

[66] N. P. Vizarim, J. C. B. Souza, C. J. O. Reichhardt, C. Reichhardt, M. V. Milošević, and P. A. Venegas, Soliton motion in skyrmion chains: Stabilization and guidance by nanoengineered pinning, Phys. Rev. B **105**, 224409 (2022).

[67] J. C. B. Souza, N. P. Vizarim, C. J. O. Reichhardt, C. Reichhardt, and P. A. Venegas, Soliton motion induced along ferromagnetic skyrmion chains in chiral thin nanotracks, J. Magn. Magn. Mater. **587**, 171280 (2023).

[68] X. Zhang, J. Xia, O. A. Tretiakov, M. Ezawa, G. Zhao, Y. Zhou, X. Liu, and M. Mochizuki, Chiral skyrmions interacting with chiral flowers, Nano Lett. **23**, 11793 (2023).

[69] J. F. Wambaugh, C. Reichhardt, C. J. Olson, F. Marchesoni, and F. Nori, Superconducting fluxon pumps and lenses, Phys. Rev. Lett. **83**, 5106 (1999).

[70] V. Vlasko-Vlasov, T. Benseman, U. Welp, and W. K. Kwok, Jamming of superconducting vortices in a funnel structure, Supercond. Sci. Technol. **26**, 075023 (2013).

[71] J. C. B. Souza, N. P. Vizarim, C. J. O. Reichhardt, C. Reichhardt, and P. A. Venegas, Clogging, diode and collective effects of skyrmions in funnel geometries, New J. Phys. **24**, 103030 (2022).

[72] R. Martinez, F. Alarcon, J. L. Aragones, and C. Valeriani, Trapping flocking particles with asymmetric obstacles, Soft Matter **16**, 4739 (2020).

[73] E. M. Gonzalez, N. O. Nunez, J. V. Anguita, and J. L. Vicent, Transverse rectification in superconducting thin films with arrays of asymmetric defects, Appl. Phys. Lett. **91**, 062505 (2007).

[74] Q. Lu, C. J. O. Reichhardt, and C. Reichhardt, Reversible vortex ratchet effects and ordering in superconductors with simple asymmetric potential arrays, Phys. Rev. B **75**, 054502 (2007).

[75] C. J. O. Reichhardt and C. Reichhardt, Vortex clogging, commensuration, and diodes in asymmetric constriction arrays, J. Supercond. Nov. Magn. **26**, 2005 (2013).

[76] J. E. Villegas, E. M. Gonzalez, M. P. Gonzalez, J. V. Anguita, and J. L. Vicent, Experimental ratchet effect in superconducting films with periodic arrays of asymmetric potentials, Phys. Rev. B **71**, 024519 (2005).

[77] K. Yu, T. W. Heitmann, C. Song, M. P. DeFeo, B. L. T. Plourde, M. B. S. Hesselberth, and P. H. Kes, Asymmetric weak-pinning superconducting channels: Vortex ratchets, Phys. Rev. B **76**, 220507(R) (2007).

[78] F. S. Wells, Investigating vortex behaviour in superconducting thin films through magnetic microscopy techniques, Ph.D. thesis, University of Wollongong, 2017, https://www.researchgate.net/publication/332514394_Investigating_Vortex_Behaviour_in_Superconducting_Thin_Films_through_Magnetic_Microscopy_Techniques?channel=doi&linkId=5cb907a1299bf120976f91ad&showFulltext=true.

[79] R. F. L. Evans, Atomistic spin dynamics, in *Handbook of Materials Modeling: Applications: Current and Emerging Materials*, edited by W. Andreoni and S. Yip (Springer International Publishing, Berlin, 2018), pp. 1–23.

[80] J. Iwasaki, M. Mochizuki, and N. Nagaosa, Current-induced skyrmion dynamics in constricted geometries, Nat. Nanotechnol. **8**, 742 (2013).

[81] S. Seki and M. Mochizuki, *Skyrmions in Magnetic Materials* (Springer International Publishing, Berlin, 2016).

[82] X. Zhang, J. Xia, and X. Liu, Particle-like skyrmions interacting with a funnel obstacle, Phys. Rev. B **106**, 094418 (2022).

[83] S. Paul, S. Haldar, S. von Malottki, and S. Heinze, Role of higher-order exchange interactions for skyrmion stability, Nat. Commun. **11**, 4756 (2020).

[84] J. C. Slonczewski, Dynamics of magnetic domain walls, AIP Conf. Proc. **5**, 170 (1972).

[85] T. L. Gilbert, A phenomenological theory of damping in ferromagnetic materials, IEEE Trans. Magn. **40**, 3443 (2004).

[86] J. Zang, M. Mostovoy, J. H. Han, and N. Nagaosa, Dynamics of skyrmion crystals in metallic thin films, Phys. Rev. Lett. **107**, 136804 (2011).

[87] Y. Araki, Magnetic textures and dynamics in magnetic Weyl semimetals, Ann. Phys. (NY) **532**, 1900287 (2019).

[88] N. Nagaosa, T. Morimoto, and Y. Tokura, Transport, magnetic and optical properties of Weyl materials, Nat. Rev. Mater. **5**, 621 (2020).

[89] See Supplemental Material at http://link.aps.org/supplemental/10.1103/PhysRevB.109.054407 for an illustration of some particular skyrmion trajectories for the systems of Figs. 3(c), 5(d), 8(d), and 10(c). The name of the videos match the corresponding figure. The animated trajectories help to better understand the skyrmion behavior under the influence of the linear protrusion array.

[90] O. Boulle, J. Vogel, H. Yang, S. Pizzini, D. de Souza Chaves, A. Locatelli, T. O. Menteş, A. Sala, L. D. Buda-Prejbeanu, O. Klein, M. Belmeguenai, Y. Roussigné, A. Stashkevich, S. M. Chérif, L. Aballe, M. Foerster, M. Chshiev, S. Auffret, I. M. Miron, and G. Gaudin, Room-temperature chiral magnetic skyrmions in ultrathin magnetic nanostructures, Nat. Nanotechnol. **11**, 449 (2016).

[91] A. Sonntag, J. Hermenau, S. Krause, and R. Wiesendanger, Thermal stability of an interface-stabilized skyrmion lattice, Phys. Rev. Lett. **113**, 077202 (2014).

[92] C. Reichhardt and C. J. O. Reichhardt, Thermal creep and the skyrmion Hall angle in driven skyrmion crystals, J. Phys.: Condens. Matter **31**, 07LT01 (2019).